



Experimental Study on Superplastic Forming for Inconel 718 Alloy Bipolar Plate

Bingxing Wang¹ · Xu Yang¹ · Wenxiang Zhu¹ · Zhuocheng Li¹ · Bin Wang¹ · Yong Tian¹

Received: 13 March 2024 / Revised: 20 August 2024 / Accepted: 21 August 2024
© The Author(s), under exclusive licence to Korean Society for Precision Engineering 2024

Abstract

With the development of the clean energy industry, higher requirements are put forward for the forming mode and service performance of bipolar plates, a key component of hydrogen fuel cells. The nickel-based alloy with corrosion and high-temperature resistance, as the potential material for bipolar plate, has the problem of insufficient plasticity. This paper proposes the superplastic forming method as a new attempt to prepare the Inconel 718 bipolar plate. The sheet with fine crystal structure exhibits excellent superplasticity at high temperatures and slow compression rate, thus forming bipolar plates with deep flow channels (~0.6 mm) and flat surfaces. The microscopic observation of the channel section shows that the straight channel at the edge is more filled due to the easier feeding of the material. Moreover, the corner channel exhibits more obvious local thinning and stress concentration than the straight channel, especially at the rounded corner of the inner turning. Increasing the billet thickness or adjusting the compression rate can improve the thickness distribution and filling effect for the product to a certain extent. Thicker sheets exhibit a lower proportion of high-stress regions during superplastic forming. Moreover, the moderate compression rate of $2 \times 10^{-3} \text{ mm s}^{-1}$ suppresses dislocation proliferation while avoiding grain growth in local areas, which improves the superplastic flow of the alloy and the quality of the final product.

Keywords Superalloy · Bipolar plate · Superplastic forming · Microstructure analysis · Microchannel structure

1 Introduction

Proton exchange membrane fuel cells (PEMFCs), with hydrogen and oxygen as fuel, are equivalent to a reverse device for electrolyzing water. Due to its advantages of high energy efficiency, low operating temperature, and environmental friendliness, PEMFCs are widely applied in transportation and other fields [1, 2]. Bipolar plates (BPPs), which account for 60–80% of the total PEMFCs weight, play an important role in supporting, conducting heat and electricity, and transporting gas [3, 4]. Recently, metal BPPs have received much attention because of their high electrical and thermal conductivity, as well as excellent machining performance [5]. Moreover, since the flow field in the metal BPPs dominates the water management and reactant distribution of PEMFCs [6], it is crucial to find the proper forming

methods to control the thickness distribution and geometric profile of flow channels.

Considering the accuracy, efficiency, and cost of the product, pressure processing such as stamping is the first choice for metal BPP manufacturing [7]. Liu et al. [8], developed a rubber pad-forming process to reduce die costs and increase efficiency. The flexible contact surface between the rigid die and the rubber improves the formability of the blank. Jin et al. [9], applied dynamic square wave loads to reduce forming defects in the stamping of stainless steel BPPs. Mohammadtabar et al. [10] proposed a double-step hydroforming to expand the forming depth and the filling percentage. The sheets were preformed by the concave die and then placed on the punch to obtain the microchannel shape. Similarly, Xu et al. [11] developed a multistage stamping to prepare titanium BPPs microchannels, thereby improving the limit aspect ratio and reducing the contact resistance. Inevitably, different types of dies need to be manufactured to suit different stamping stages. Kargar-Pishbijari et al. [12] conducted hot metal gas forming research on AA1070 alloy. With the increase in temperature, the formability of sheets in the microchannel mold increases, and the fracture at the

✉ Xu Yang
a2428319997@163.com

¹ State Key Laboratory of Rolling and Automation (RAL),
Northeastern University, Shenyang 110819, China

groove corner decreases. Moreover, Esmaeilpour et al. [13] proposed a variety of 3D yield functions to account for normal and shear stress components, and the user material subroutine was written to simulate the single-point incremental forming of aluminum alloy sheets. Esmaeilpour et al. [14] used a 3D representative volume element and a crystal plasticity model to generate out-of-plane stresses for calibrating the Yld2004-18p yield function, enabling accurate simulation of incremental sheet forming.

The forming method mentioned above is suitable for alloys with excellent plasticity, such as some aluminum alloys, titanium alloys, and stainless steel. However, for hard-to-deform metals, although progressive forming or heating is used to improve traditional stamping, the BBPs are still prone to defects such as rebound, cracking, and folding due to the poor plasticity of the raw material [15]. With the advantages of low stress, easy forming, no rebound and no necking, superplastic forming (SPF) is an effective method to enhance the formability of alloys [16]. SPF has been widely used in the automobile and aerospace fields. For instance, Tang et al. [17], modified hot bending assisted gas forming to manufacture aero-industrial strakelet. Yi et al. [18], developed the reverse direction two-stage SPF process to prepare the AA5083 alloy door frame. Therefore, SPF has the potential to manufacture complex thin-walled parts such as BBPs in a single process [19]. At present, only Choitotin et al. [20] have conducted preliminary studies in this field: AA5052 alloy BBPs were formed at a low pressure of 1 MPa by gas blowing. However, the relevant processes were introduced in this study without discussing the effect of specific parameters on the product geometry.

Recently, Zhong et al. [21], pointed out that commercial nickel-based superalloys are candidate materials for the preparation of non-coated BBPs due to their better corrosion resistance. However, common superalloys such as Inconel 718 have serious strain hardening tendency and difficulty in forming at room temperature [22, 23]. Therefore, it is a feasible attempt to fabricate BBPs by using the superplasticity of fine-grained superalloys at high temperatures. In this paper, the SPF of Inconel 718 BBPs was achieved by the combination of induction heating and mechanical compression. The effects of initial sheet thickness and compression

rate on the geometrical size and microstructure of the flow channel were investigated in detail. Moreover, the existing research about BBPs forming mainly focuses on the straight channel (SC) but neglects the manufacturing quality of the corner channel (CC) and the structure difference at different positions. This paper discussed the dimensional variation of channels from the edge to the center of the BBPs. The microstructure and profile of CCs were also analyzed with emphasis.

2 Experimental Procedures

2.1 Experimental Materials

The fine and uniform grain structure is the prerequisite for the materials to obtain superplasticity. The initial sheets with thicknesses of 0.08, 0.14, and 0.19 mm were prepared by cold rolling and two-stage annealing [24]. The average grain size and δ phase content of the sheet are 1.63 μm (without counting the twin boundary) and 7.12%, respectively, as shown in Fig. 1a and b.

2.2 Superplastic forming experiment

The BBPs with a single serpentine channel were prepared by superplastic compression. Figure 2a shows the schematic diagram of thermoforming equipment. The specific steps include: (1) The sheet and die were placed inside the compressor after assembly; (2) The high-frequency current was passed through external fixed coils to achieve the induction heating of the dies and alloy sheets (precise temperature control via infrared) [25]; (3) The punch was slowly compressed with the drop rate set by the computer until the specified force was reached; (4) The BBPs were taken out for water cooling and slight pickling after compression stopped. Figure 2b and b1 display the appearance photos of the dies and the geometry of the channel section, respectively. The geometrical dimensions of the micro-channel include external fillet radius (R), internal fillet radius (r), draft angle (α), flow channel depth (h), flow channel width (w), and rib width (s). According to previous studies [26, 27], the alloy exhibits

Fig. 1 a Matrix structure and b δ phase distribution of the initial sheets

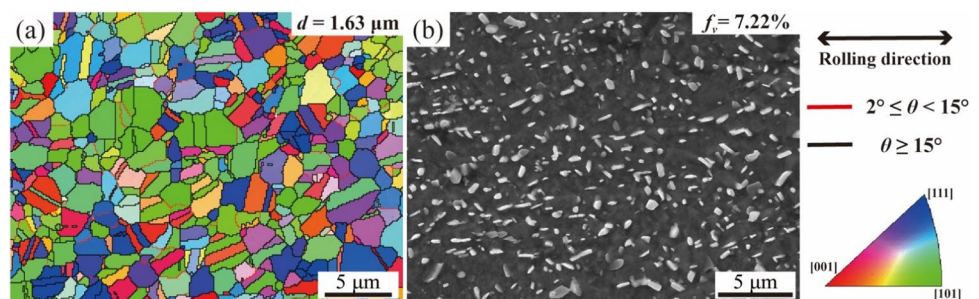
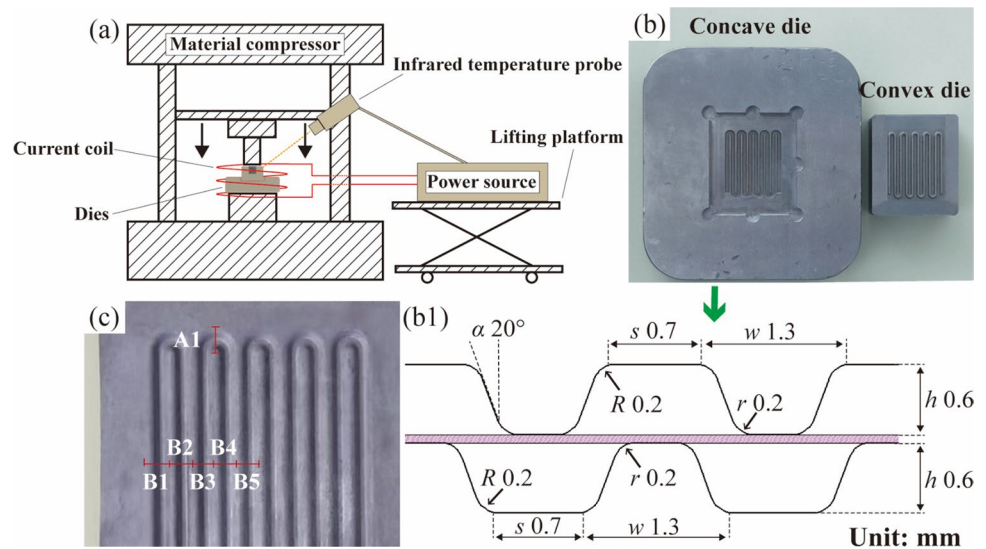


Fig. 2 **a** Schematic diagram of experimental equipment. **b** Macroscopic picture of the dies used for thermal compression. **b1** Key geometric parameters of the longitudinal section of the dies. **c** Section position for microscopic inspection



the highest superplastic elongation at approximately 950 °C. Therefore, the sheets with different thicknesses (i.e., 0.08, 0.14, and 0.19 mm) were compressed at 950 °C with punch drop rates (V) of 5×10^{-4} , 2×10^{-3} and 1×10^{-2} mm s⁻¹. The high temperature and slow descent rate ensured that the alloy remained in the superplastic state during deformation. Moreover, the threshold stress was set to a lower value of 20 kN, and the forming process ended when the compressive stress reached this value.

2.3 Analysis of Geometric Size and Microstructure

Optical microscopy (OM, BX53M), hardness tester (HV, FM-700E), and electron backscatter diffraction (EBSD, ZEISS ULTRA PLUS) were used to analyze the microstructure characteristics and mechanical behavior at different locations of BBPs. Two types of sections were selected for observation: CC (i.e., A1) and SC (i.e., B1–B5), as shown in Fig. 2c. The OM samples were cut with an electric spark cutter, then ground on sandpaper and mechanically polished with water. Subsequently, the microhardness test was performed with a load of 200 kgf mm⁻² and a holding time of 10 s. The samples for EBSD were electropolished in a solution of 90% CH₃CH₂OH + 10% HClO₄ at 30 V for 15 s. Detailed test locations for EBSD and microhardness are described in the results.

3 Results and Discussion

3.1 Macroscopic Morphology of Bipolar Plate

Figure 3 shows the morphology of the products after SPF and conventional stamping at specific conditions, respectively. The results show that the products prepared by

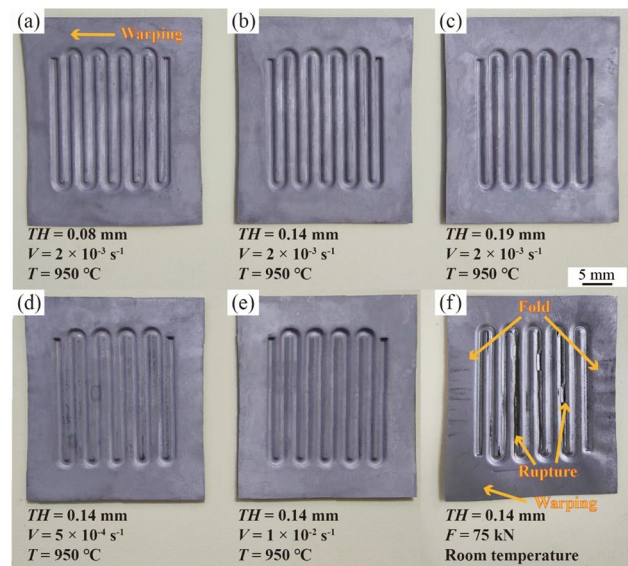


Fig. 3 **a–e** The morphology of BPPs prepared at 950 °C with different initial sheet thickness (TH) and compression rate. **f** The morphology of the BPP after stamping at 75kN at room temperature

SPF have a smooth surface and clear profile. In addition, the thinner thickness causes slight warping at the edges (Fig. 3a). However, the stamping at room temperature requires a greater forming pressure of 75 kN and leads to serious cracking of the BPPs (Fig. 3f). The apparent folding and warping at the edges also interfere the practical performance of the product. Therefore, compared with traditional stamping, SPF through slow-rate compression and induction heating is a feasible way to produce superalloy BPPs. In the following, the effect of thickness on forming is studied through detailed microscopic analysis for products (a), (b), and (c). Moreover, the role of

compression rates is described in Sect. 3.3 by comparing samples (b), (d), and (e).

3.2 Effect of Initial Thickness on Superplastic Forming

3.2.1 Straight Channel Section

Figure 4 shows the thickness distribution at the SC section of BPPs prepared by sheets with different thicknesses. There are obvious differences in thickness fluctuation at channels B1 and B5, which are reflected in the number of thinning zones. The asymmetric thickness distribution at channel B1 shows the slight thinning region I at the right fillet (Fig. 4a and a1). However, channel B5 has obvious symmetric thinning regions II and III on both sides (Fig. 4b and b1). The results suggest uneven deformation for the BPPs in each flow channel during SPF. The bottom fillets are subjected to direct pressure from the punch. Moreover, due to the friction between the billet and the die, it is difficult for the bottom material to feed into the wall on both sides. However, compared to channel B5, the left side of channel B1 is a free boundary rather than a deformation region. The flow and filling of materials in the superplastic state inhibits the thinning of this region. Moreover, the more severe thinning of the B5 channel indicates that the feed and flow of materials are difficult in areas closer to the center of the BPP.

To illustrate the change in sheet thickness after the SPF process, the thinning percentage P_{th} and average thickness error e_{th} at different channels are shown in Fig. 4c and d, respectively. The thinning percentage is calculated as follows [12].

$$P_{th} = \frac{TH - th_{\min}}{TH} \times 100\% \quad (1-1)$$

where TH is the initial sheet thickness and th_{\min} is the minimum thickness of a channel. The average thickness error reflects the thickness fluctuations at different locations for a channel, and its specific expression is

$$e_{th} = \frac{SD}{th} \times 100\% \quad (1-2)$$

where SD and th are the standard deviations and average value of the thickness data at a channel, respectively. Compared with channel B1, channel B5 shows more obvious thinning and thickness error (Fig. 4c and d), which is caused by poor material fluidity in the central region. In addition, the thickness fluctuation and thinning percentage for products at different SC sections decrease with the increase of the initial sheet thickness. Especially when the billet thickness increases from 0.08 to 0.14 mm, the uniformity of channel thickness is dramatically reduced. The results show that it is

difficult for thin billets to adapt to local severe deformation because of the lack of material in the thickness direction.

Figure 5 shows the geometry and microhardness information at SC sections for the BPPs with different thicknesses. The forming depth at channel B1 reaches the setting value of the die (i.e., 0.6 mm), higher than at channels B2–B5, as displayed in Fig. 5a. Moreover, channel B1 exhibits a better aspect ratio and fill percentage than other channels (Fig. 5b and c). The aspect ratio is defined as the ratio of the depth d_e to the length of the median line w_1 , as shown in Fig. 5b1. The increase in aspect ratio is conducive to uniform heat and mass transfer for BPPs, which further improves the efficiency and performance of PEMFC [11]. With the red dotted line as the common boundary, the filling percentage refers to the ratio of the area enclosed by the external outline of sheets A_a to the total area of concave die A_r (Fig. 5c1). Consistent with the previous analysis, the B1 channel appears good formability because the free boundary reduces the tension stress concentration at the bottom fillet.

As displayed in Fig. 5d, the microhardness (i.e., the average microhardness of the points marked in Fig. 5d1) increases as the channel location moves closer to the center of the BPP, indicating significant work hardening in the central region. During superplastic compression, the central region is in a higher tensile stress state than the sheet edge, especially in the area of local thinning such as the wall and lower fillet. (Fig. 4b and b1) [28]. In these high-stress regions, the superplastic deformation mechanism of the alloy changes from grain boundary slip (GBS) to intragranular dislocation creep, causing an increase in dislocation density [29]. Since material strength is generally proportional to microhardness [30], it can be inferred that channels B3 and B5 have higher strength than channel B1. Moreover, the increase in the initial thickness has little effect on the channel depth (Fig. 4a). Therefore, SPF can enable billets with different thicknesses to reach the desired shape even at a lower pressure (20 kN). The aspect ratio and filling percentage of each channel increase slightly with the increase of the initial thickness (Fig. 4b and c). This is because, in the case of similar depths, these two indicators are mainly related to the thickness of the channel wall, with thicker walls leading to a larger outer profile and a smaller width at half depth (i.e., w_1).

3.2.2 Corner Channel Section

Figure 6 shows the geometric characterization at CC sections for the BPPs prepared from sheets with different thicknesses. There are two asymmetrical thinning regions at the CC section: the severe thinning region at the upper left fillet (zone I) and the slight thinning region at the lower right fillet (zone II, which is similar to Fig. 4a and b). This experimental result can be explained by the simulation analysis of Wang

et al. [28]. The materials at the turning interact with each other because of the strain continuity. At the outer turning (point N, Fig. 6a1), the radius of the circular arc decreases with the decrease of the height, and there is mutual extrusion between the materials, leading a certain compressive stress. However, the increasing arc radius with decreasing height at

the M point of the inner turning (Fig. 6a1) can cause a large tensile stress between the materials and lead to severe local deformation. Therefore, the equivalent strain at point M is greater than at point N, which is consistent with our previous simulation results [31]. Moreover, as the billet thickness increases from 0.08 to 0.14 mm, the thickness uniformity

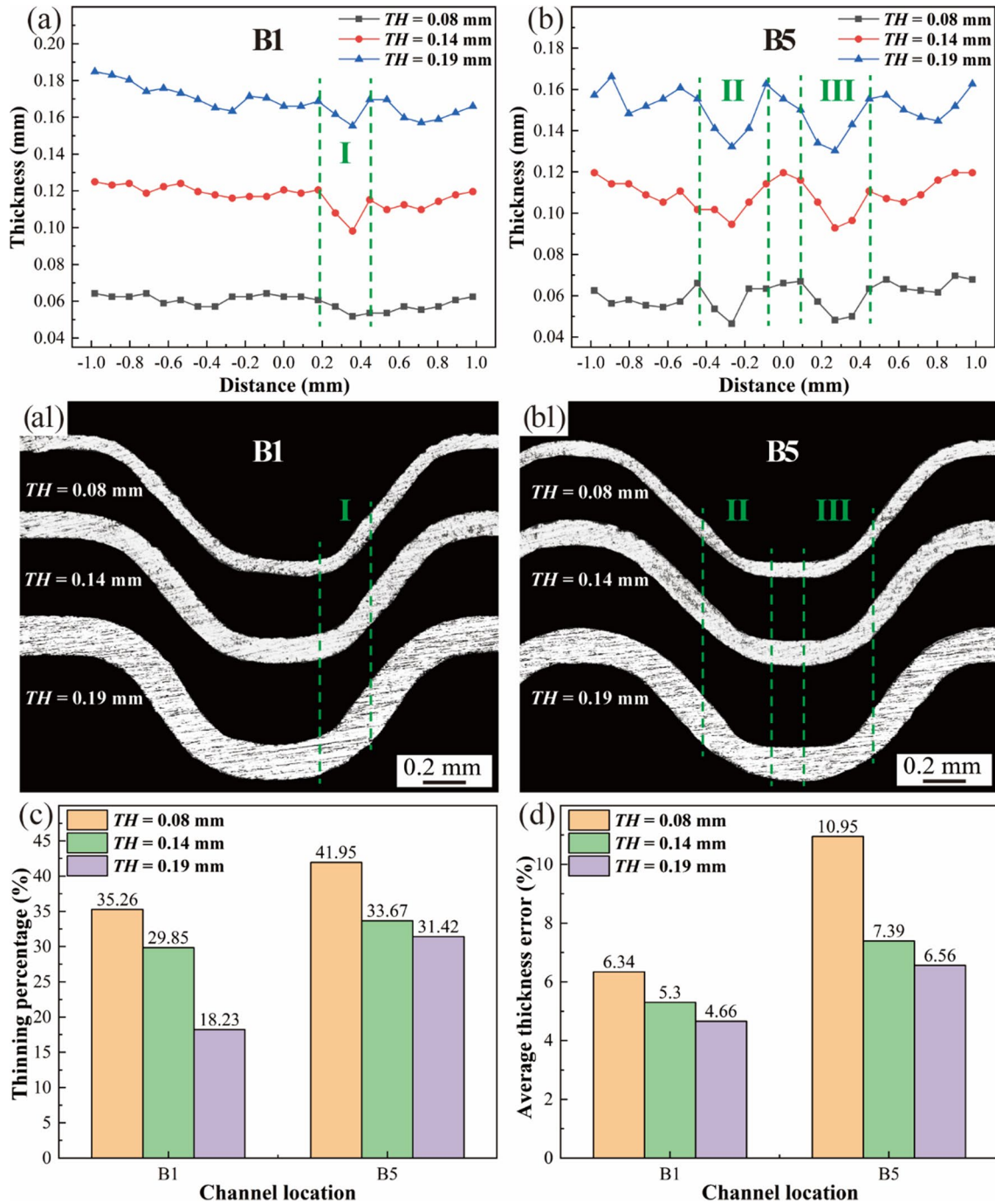


Fig. 4 Thickness distribution at channels B1 and B5 for the BBPs with different initial thicknesses: the changes of thickness with location at channels **a** B1 and **b** B5; **a1**, **b1** the corresponding profile pho-

tos; **c** thinning percentage and **d** average thickness error at different channels, respectively

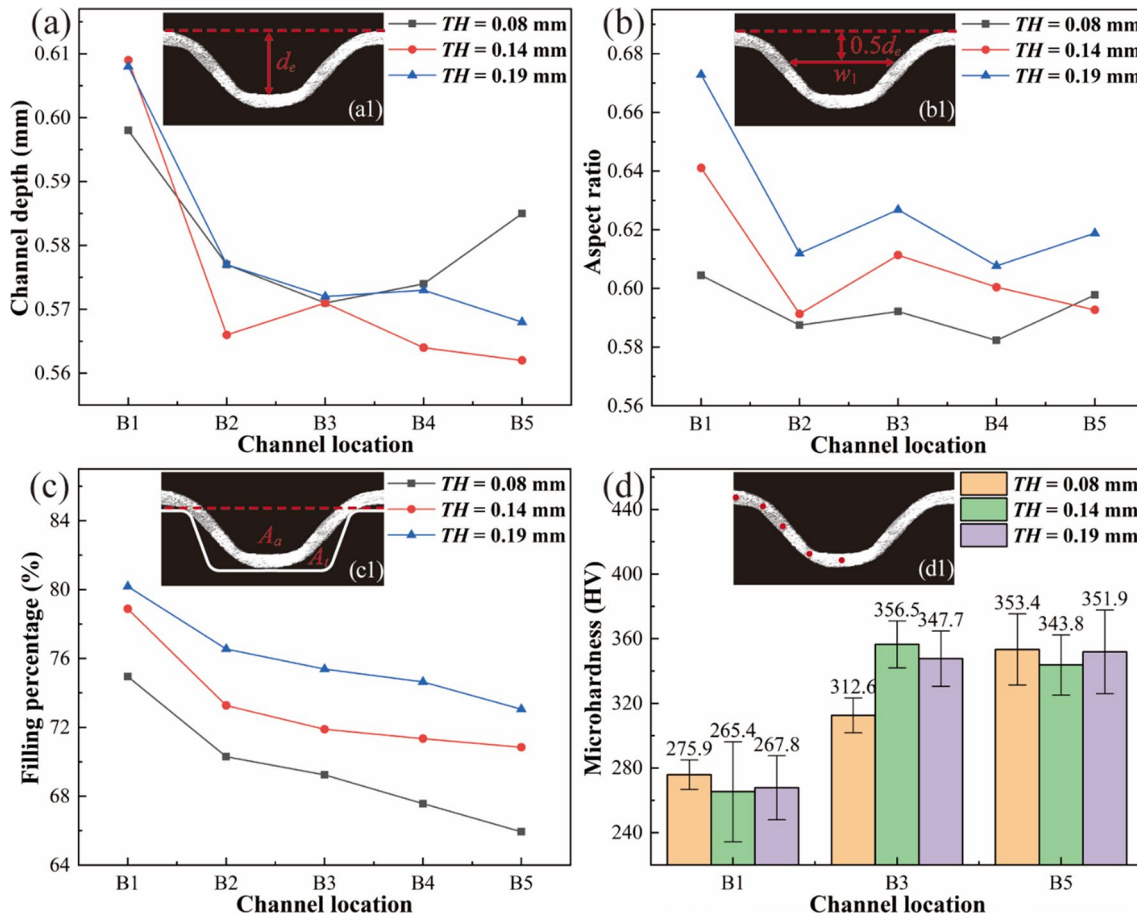


Fig. 5 The changes in **a** channel depth, **b** aspect ratio, **c** filling percentage, and **d** microhardness at the SC section for BPPs with different initial thicknesses. The embedded (a1)–(d1) illustrate the calculation method for each data type

and filling effect for the CC are significantly improved. Still, the change of these indicators is not obvious when the initial thickness is further increased to 0.19 mm (Fig. 6c, d, and e).

The experimental results in Figs. 4, 5 and 6 show that the SPF-prepared BPPs have more serious thickness thinning and size fluctuation at the CCs. Increasing the billet thickness has a certain effect on enhancing the thickness uniformity and filling capacity of the final product. The severe thinning zones during the SPF process are in a relatively high-stress state. According to the analysis by Zhang et al. [17], with the increase of the initial thickness, the relative proportion of the high-stress zone decreases and the low-stress zone expands at the side wall, resulting in the uniform distribution of the overall stress. For BPPs with an initial thickness of 0.08 mm, most of the walls on both channel sides are in a high-stress state, especially in the inner wall of channel A1 (Fig. 6a1). In this high-stress region, the superplastic deformation mechanism changes from GBS to dislocation creep independent of grain size, which reduces the local material fluidity [16]. Insufficient material feed and high deformation resistance lead to incomplete filling at this location, as shown by the orange arrow (Fig. 6a1).

Although a moderate increase in thickness improves the forming quality of BPPs, it is necessary to consider the functional characteristics, material cost, and product weight to obtain the optimal solution.

As reported by Aue-U-Lan et al. [32], the ultimate thinning percentage P_{\max} (i.e., the material is in a critical failure state) is expressed as follows.

$$P_{\max} = 1 - \exp(\varepsilon_t) \quad (3)$$

where ε_t represents thickness strain and it is calculated by Eqs. (4) and (5).

$$\varepsilon_t = -\varepsilon_r = -\ln(1 + e_r/100) \quad (4)$$

$$e_r = \frac{23.3 + 360TH/25.4}{0.21m} \quad (5)$$

where e_r and ε_r are the engineering major strain and main true strain at plane-strain condition, respectively; TH and m denote the initial thickness of the sheet and strain rate sensitivity index (i.e., the inverse of the stress index n),

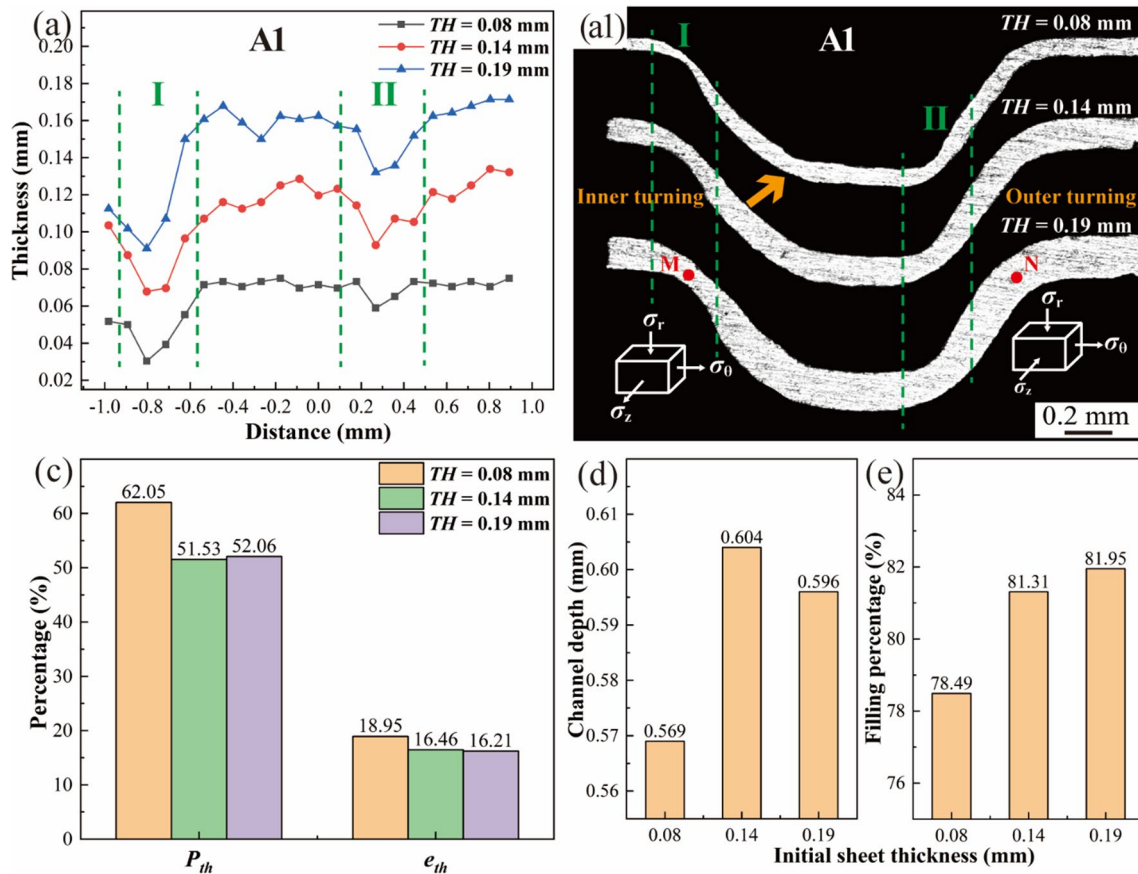


Fig. 6 The geometric characterization at the CC section for the BPPs with different initial thicknesses: **a** thickness changes with location and (a1) corresponding profile photos; **b** thinning percentage and

average thickness error; the changes in **(c)** channel depth and **(d)** filling percentage with the initial sheet thickness

respectively. According to our previous studies [23], the m value of superplastic Inconel 718 alloy at 950 °C is approximately 0.383. For sheets with different initial thicknesses, the calculated failure thinning rate is in the range of 75.23% to 76.37%, which is higher than the most severe thinning at the CC Sect. (62.05%, Fig. 6c). Therefore, the high critical thinning for the superplastic material can avoid fracture due to severe local deformation.

3.3 Effect of Compression Rate on Superplastic Forming

3.3.1 Geometric Dimension Analysis

Figure 7a and a1 illustrates the thickness distribution at the SC section for the BPPs under different punch drop rates. For all products, the thickness of channel B5 changes from the center to the two sides in a V-shape. The most severe thinning is located at the lower fillet as indicated by the dotted green line, which is consistent with the analysis in Fig. 4a. BPPs prepared by different processes appear

similar thickness distribution at channel B5, indicating that the compression rate has little effect on improving the local thickness at SCs. Figure 7b–e shows the channel size and microhardness at the SC section for the BPPs compressed at different rates. At higher or lower compression rates, the channel depth, aspect ratio, and filling percentage decrease as the channel is closer to the center of the sheet (Fig. 7b, c, and d). By contrast, the BPPs prepared with a punch drop rate of $2 \times 10^{-3} \text{ mm s}^{-1}$ exhibit better dimensional stability at channels B2–B5. The high strain rate causes the proliferation and entanglement of dislocations in the alloy, which further promotes work hardening and local necking [33]. Moreover, the obvious grain growth at low strain rates is also detrimental to the GBS behavior due to the decrease in grain boundary density [34]. Therefore, a moderate rate maintains the stable superplastic flow of the alloy, which promotes the mutual feeding of channels located in the central region (i.e., B2–B5). Figure 7d shows that the microhardness for each channel decreases with the decrease in compression rate. The lower strain rate reduces the amount of plastic deformation per unit time. Therefore, sufficient time allows

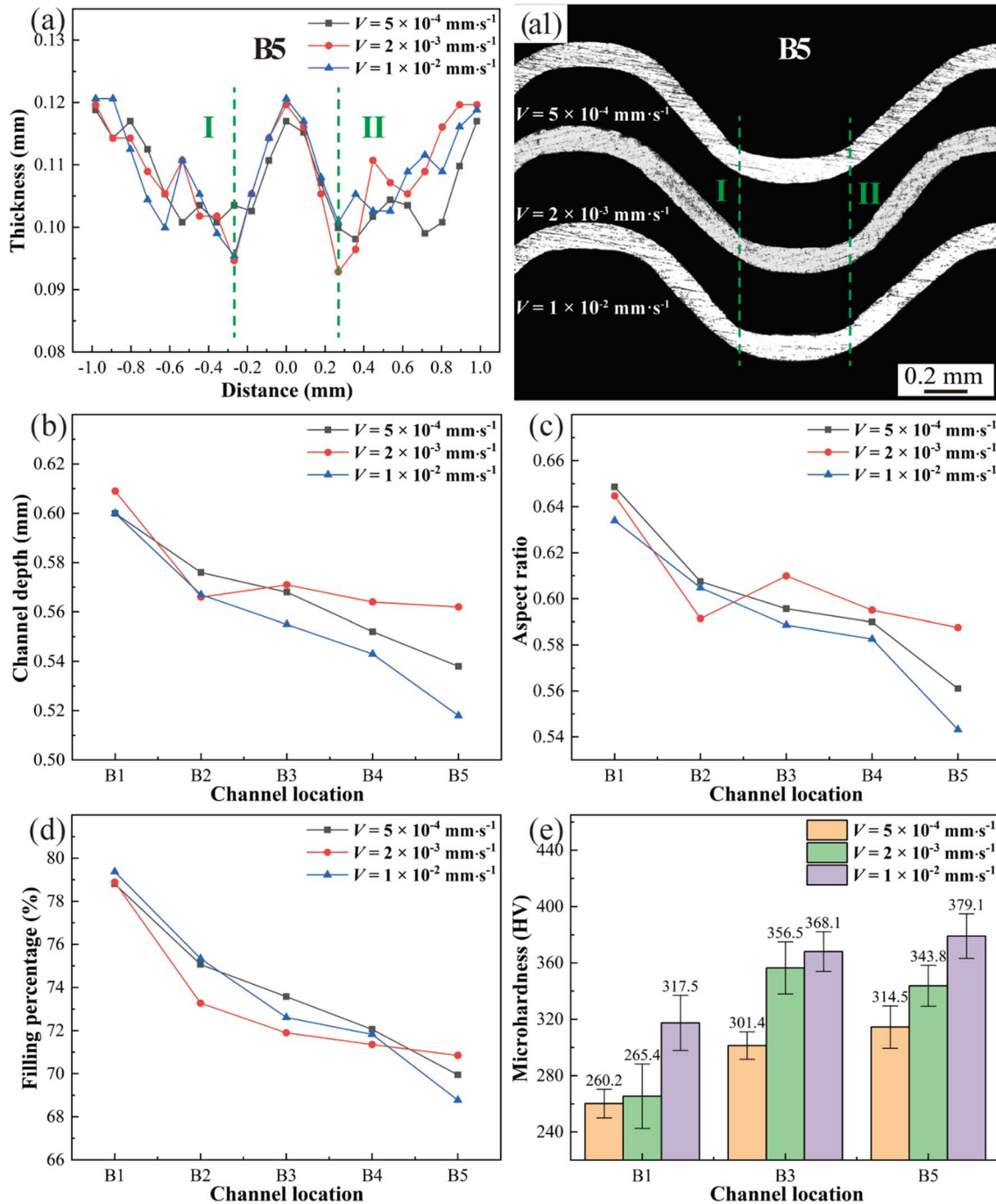


Fig. 7 The geometric characteristics and microhardness at the SC section for the BPPs compressed at different rates: **a** thickness change with location and **a1** the corresponding profile photos for channel B5;

the changes in **b** channel depth, **c** aspect ratio, **d** filling percentage and **e** microhardness at different channels. The calculation method for each data type is the same as in Fig. 5

for dynamic recovery of the material to reduce dislocation density and work hardening [35].

Figure 8 shows the geometric characterization at CC sections for the BPPs prepared under different punch drop rates. Similar to the results in Fig. 6, all channel walls are narrowed at positions I and II (Fig. 8a and a1). At a higher

compression rate of $1 \times 10^{-2} \text{ mm s}^{-1}$, the BPPs exhibit drastic thinning and jagged damage at position I, as shown by the orange arrow in Fig. 8a1. Therefore, this forming condition results in relatively poor thickness uniformity at CCs (Fig. 8c). The higher strain rate causes more severe stress concentration and microcrack initiation in the position I (and

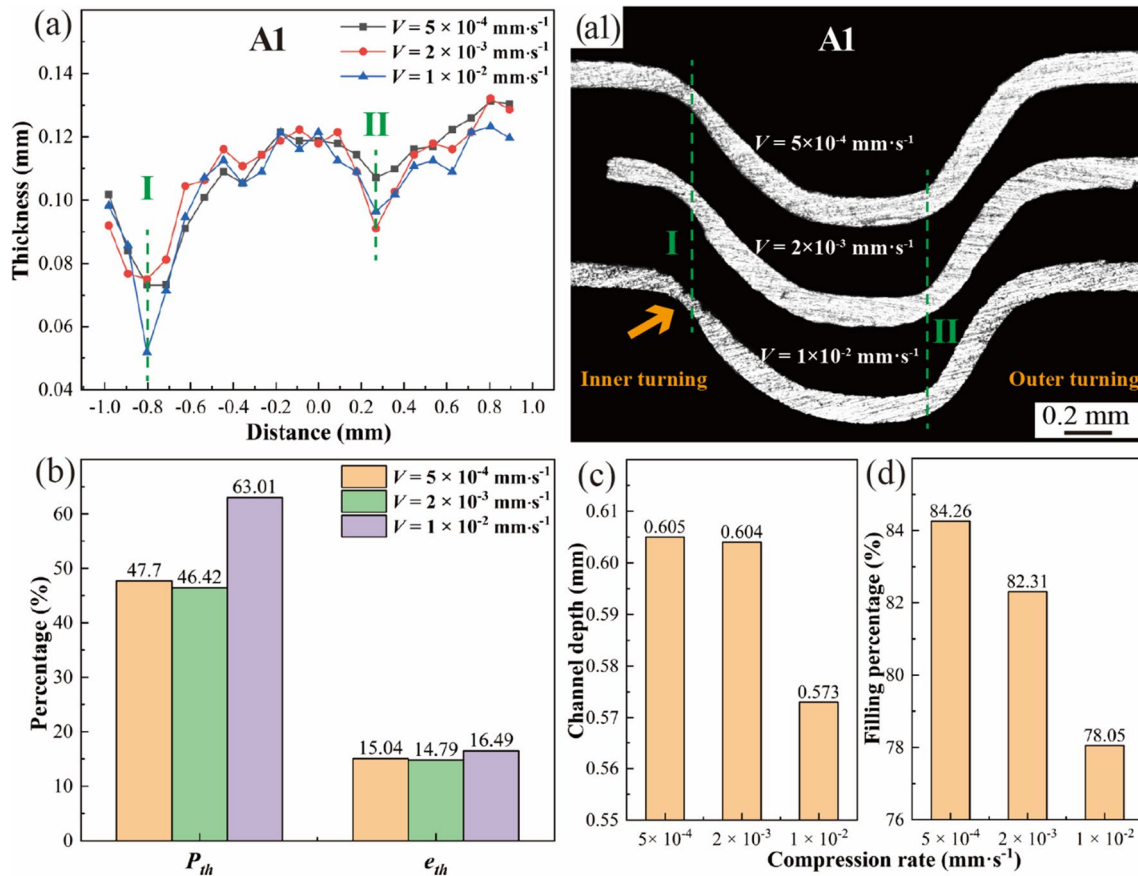


Fig. 8 The geometric characterization at CC sections for the BBPs compressed at different rates: **a** thickness changes with location and **(a1)** corresponding profile photos; **b** thinning percentage and average

thickness error; the changes in **c** channel depth and **d** filling percentage with the compression rate

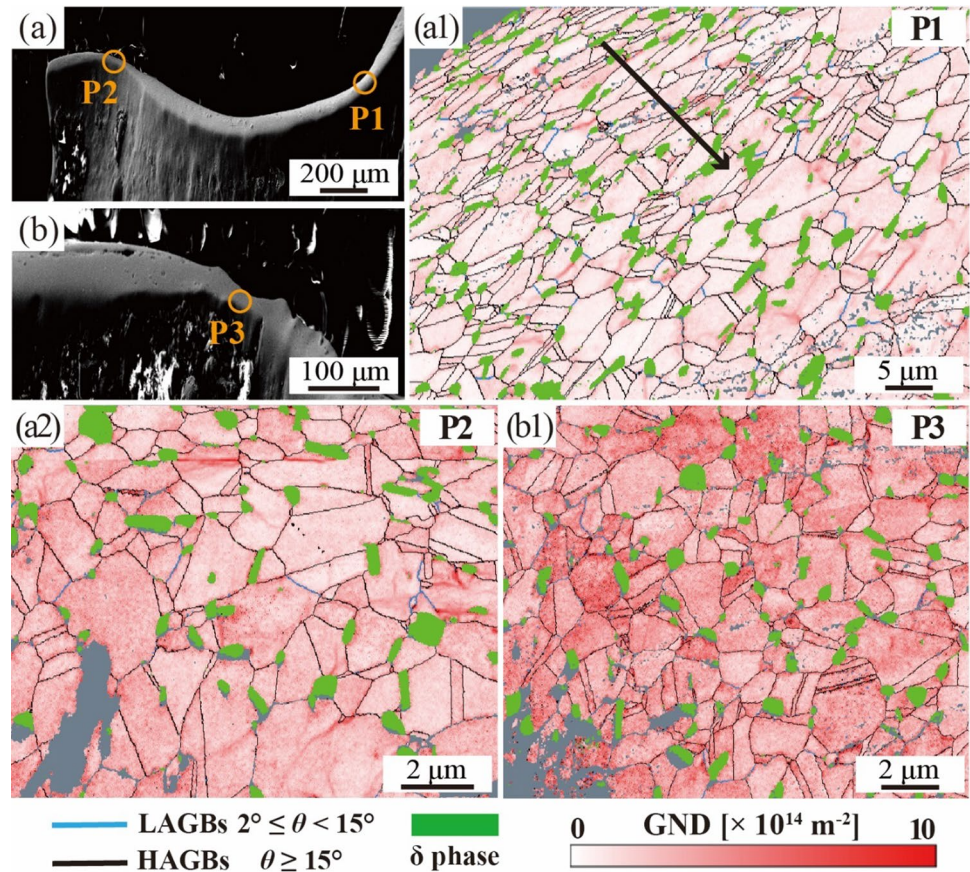
the surrounding channel wall) [36]. Moreover, large-scale dislocation proliferation in these regions increases forming resistance, thereby reducing the channel depth and filling percentage (Fig. 8d and e). Similar SPF results are obtained for channel A1 under medium and low compression rates (Fig. 8c and d). Because of higher stress levels at CCs compared to SCs, sufficient time is required for dynamic recovery to relieve severe work hardening at the CC section [37]. Therefore, the optimal compression rate for channel A1 may be lower on the whole than for channels B1–B5.

3.3.2 Analysis of Microstructure Evolution

The work hardening of materials is generally estimated by the geometric necessity dislocation (GND) density associated with non-uniform plastic deformation [38]. Figure 9 shows the SEM and GND maps of channel A1 under different compression rates. The upper surface of the P1 zone is squeezed due to contact with the dies, thus forming a fine and elongated grain structure (Fig. 9a and a1). There is a gradient change in grain size from the edge to the center, as

shown by the black arrow. Therefore, the slight reduction in thickness here (Fig. 8a1) is due to the pressure and friction of the die, which is consistent with the above analysis. Table 1 shows the average GND values and average grain sizes for different regions. Compared with region P1, there is more obvious dislocation accumulation and grain coarsening at P2 (Fig. 9a2). This proves that higher tensile stress is concentrated at the rounded corner near the inside wall, causing severe thinning in this area (Fig. 8a1). Moreover, deformation-induced grain growth leads to an increase in grain size in the region P2 [39]. By comparing regions P2 and P3 (both at the fillet on the top left), it can be found that the compression rate of $1 \times 10^{-2} \text{ mm}\cdot\text{s}^{-1}$ further promotes work hardening at this location (Fig. 8a2 and b1, Table 1). Under this condition, the SPF of the alloy is dominated by intragranular deformation associated with dislocation motion. The short duration of deformation makes the dislocation difficult to remove by dynamic recovery or climbing, which explains the cracking seen in Fig. 8a1. Because reducing the strain rate inhibits dislocation proliferation but also causes grain growth (Table 1), it is necessary to select

Fig. 9 The microstructure picture at CC sections for the BBPs compressed at different rates: SEM images of channel A1 under compression rates of (a) 2×10^{-3} and (b) $1 \times 10^{-2} \text{ mm s}^{-1}$; (a1), (a2), and (b1) are GND micrographs at the corresponding marks in Fig. 9a and b, respectively



a suitable compression rate to control the external geometry and internal microstructure.

The results show that the higher compression rate (i.e., $1 \times 10^{-2} \text{ mm s}^{-1}$) not only reduces the uniformity of thickness and depth but also causes large residual stress in local locations, which affects the performance and service life of the product [9]. A slower compression rate (i.e., $5 \times 10^{-4} \text{ mm s}^{-1}$) hardly improves the uniformity of the channel structure, but significantly reduces production efficiency. Therefore, considering the microstructure and geometry of the product, it is more appropriate to set the compression rate at approximately $2 \times 10^{-3} \text{ mm s}^{-1}$. In this study, increasing the initial thickness or adjusting the compression rate can somewhat improve the local thinning at the fillets. Moreover, the BBPs prepared by SPF can be further optimized by changing the

structure of dies such as the radius of the inner and outer fillets. This part of the research needs to be further in-depth.

4 Conclusion

This paper presents a superplastic compression method for preparing Inconel 718 alloy BPPs. The effects of sheet thickness and compression rate on the geometrical size and local microstructure of the final product are studied in detail. The relevant important viewpoints are summarized as follows.

1. The SPF by slow compression and induction heating is an effective way to produce superalloy BPPs with deep channels and flat surfaces. At lower forming pressures, the SPF process can achieve a maximum thinning rate of 62.05% and a filling percentage of more than 78%. The flow channels in the central area of BPPs exhibit poor thickness homogeneity and filling capacity due to less material supply and obvious work hardening.
2. The CC exhibits more obvious local deformation and stress concentration than the SC, especially at the rounded corner of the inner turning. The lower billet thickness of 0.08 mm increases the high-stress area and

Table 1 Statistics of average GND density and average grain size at different locations

Location	P1	P2	P3
Average GND density ($\times 10^{14} \text{ m}^{-2}$)	1.25 ± 0.8	2.64 ± 1.33	3.65 ± 1.78
Average grain size (μm)	1.68 ± 0.52	1.96 ± 0.62	1.64 ± 0.55

inhibits the GBS process during SPF. Proper increase of billet thickness can optimize thickness distribution and channel structure for products.

- The moderate compression rate of $2 \times 10^{-3} \text{ mm s}^{-1}$ can improve the forming uniformity for different SCs and the severe deformation at the CCs. The higher compression rate increases the stress concentration and dislocation accumulation at the channel wall and the fillet, resulting in local damage at CCs. The lower strain rate promotes obvious grain growth and reduces production efficiency.

Author contributions Bingxing Wang: methodology, writing-original draft. Xu Yang: writing-review & editing. Wenxiang Zhu: experimental operation. Zhuocheng Li: formal analysis. Bin Wang: project administration. Yong Tian: supervision.

Funding The authors acknowledge the financial support of the State Key Laboratory of Rolling and Automation (RAL).

Declarations

Competing interests The authors declare that they have no known competing financial interests or personal relationships that could have appeared to influence the work reported in this paper.

References

- Leng, Y., Ming, P. W., Yang, D. J., & Zhang, C. M. (2020). Stainless steel bipolar plates for proton exchange membrane fuel cells: Materials, flow channel design and forming processes. *Journal of Power Sources*, 451, 227783. <https://doi.org/10.1016/j.jpowsour.2020.227783>
- Huynh, T., Pham, A. T., Lee, J., & Nguyen-Xuan, H. (2024). Optimal parametric design of fuel cell hybrid electric vehicles by balancing composite motion optimization. *International Journal of Precision Engineering and Manufacturing-Green Technology*, 11, 123–143. <https://doi.org/10.1007/s40684-023-00526-3>
- Xu, Z., Qiu, D., Yi, P., Peng, L. F., & Lai, X. M. (2020). Towards mass applications: A review on the challenges and developments in metallic bipolar plates for PEMFC. *Progress in Natural Science: Materials International*, 30(6), 815–824. <https://doi.org/10.1016/j.pnsc.2020.10.015>
- Wang, Y., Leung, D. Y. C., Xuan, J., & Wang, H. Z. (2016). A review on unitized regenerative fuel cell technologies, part-A: Unitized regenerative proton exchange membrane fuel cells. *Renewable and Sustainable Energy Reviews*, 65, 961–977. <https://doi.org/10.1016/j.rser.2016.07.046>
- Fetohi, A. E., Hameed, R. M. A., El-Khatib, K. M., & Souay, E. R. (2012). Study of different aluminum alloy substrates coated with Ni–Co–P as metallic bipolar plates for PEM fuel cell applications. *International Journal of Hydrogen Energy*, 37(14), 10807–10817. <https://doi.org/10.1016/j.ijhydene.2012.04.066>
- Lim, B. H., Majlan, E. H., Daud, W. R. W., Husaini, T., & Rosli, M. I. (2016). Effects of flow field design on water management and reactant distribution in PEMFC: A review. *Ionics*, 22, 301–316. <https://doi.org/10.1007/s11581-016-1644-y>
- Xu, S., Li, K., Wei, Y., & Jiang, W. C. (2016). Numerical investigation of formed residual stresses and the thickness of stainless steel bipolar plate in PEMFC. *International Journal of Hydrogen Energy*, 41(16), 6855–6863. <https://doi.org/10.1016/j.ijhydene.2016.03.005>
- Liu, Y., & Hua, L. (2010). Fabrication of metallic bipolar plate for proton exchange membrane fuel cells by rubber pad forming. *Journal of Power Sources*, 195(11), 3529–3535. <https://doi.org/10.1016/j.jpowsour.2009.12.046>
- Jin, C. K., Koo, J. Y., & Kang, C. G. (2014). Fabrication of stainless steel bipolar plates for fuel cells using dynamic loads for the stamping process and performance evaluation of a single cell. *International Journal of Hydrogen Energy*, 39(36), 21461–21469. <https://doi.org/10.1016/j.ijhydene.2014.04.103>
- Mohammadtabar, N., Bakhshi-Jooybari, M., Hosseinipour, S. J., & Gorji, A. H. (2016). Feasibility study of a double-step hydro-forming process for fabrication of fuel cell bipolar plates with slotted interdigitated serpentine flow field. *The International Journal of Advanced Manufacturing Technology*, 85, 765–777. <https://doi.org/10.1007/s00170-015-7960-y>
- Xu, Z., Li, Z., Zhang, R., Jiang, T. H., & Peng, L. F. (2021). Fabrication of micro channels for titanium PEMFC bipolar plates by multistage forming process. *International Journal of Hydrogen Energy*, 46(19), 11092–11103. <https://doi.org/10.1016/j.ijhydene.2020.07.230>
- Kargar-Pishbijari, H., Hosseinipour, S. J., & Aval, H. J. (2020). A novel method for manufacturing microchannels of metallic bipolar plate fuel cell by the hot metal gas forming process. *Journal of Manufacturing Processes*, 55, 268–275. <https://doi.org/10.1016/j.jmapro.2020.04.040>
- Esmailpour, R., Kim, H., Park, T., Pourboghrat, F., & Mohammed, B. (2017). Comparison of 3D yield functions for finite element simulation of single point incremental forming (SPIF) of aluminum 7075. *International Journal of Mechanical Sciences*, 133, 544–554. <https://doi.org/10.1016/j.ijmecsci.2017.09.019>
- Esmailpour, R., Kim, H., Park, T., Pourboghrat, F., Xu, Z., Mohammed, B., & Abu-Farha, F. (2018). Calibration of Barlat Yld 2004–18P yield function using CPFEM and 3D RVE for the simulation of single point incremental forming (SPIF) of 7075-O aluminum sheet. *International Journal of Mechanical Sciences*, 145, 24–41. <https://doi.org/10.1016/j.ijmecsci.2018.05.015>
- Kwon, H. J., Jeon, Y. P., & Kang, C. G. (2013). Effect of progressive forming process and processing variables on the formability of aluminium bipolar plate with microchannel. *The International Journal of Advanced Manufacturing Technology*, 64, 681–694. <https://doi.org/10.1007/s00170-012-4033-3>
- Kawasaki, M., & Langdon, T. G. (2016). Achieving superplastic properties in ultrafine-grained materials at high temperatures. *Journal of Materials Science*, 51, 19–32. <https://doi.org/10.1007/s10853-015-9176-9>
- Tang, J. S., Fuh, Y. K., & Lee, S. (2015). Superplastic forming process applied to aero-industrial strakelet: Wrinkling, thickness, and microstructure analysis. *The International Journal of Advanced Manufacturing Technology*, 77, 1513–1523. <https://doi.org/10.1007/s00170-014-6527-7>
- Yi, L., Li, X., Li, Y., Yu, G., Tang, Z. M., & Gu, Z. W. (2021). Investigation of the two-stage SPF process of aluminum alloy door frames. *Journal of Materials Research and Technology*, 15, 2873–2882. <https://doi.org/10.1016/j.jmrt.2021.09.110>
- Zhang, C. Z., Yang, X., Ma, K. J., Wang, Y. H., Liu, Z. P., Liu, Z. J., & Zhang, W. J. (2021). Superplastic flow and deformation mechanism of the rolled Al–Mg–Li–Sc–Zr alloy with banded microstructure. *Metals*, 11(3), 404. <https://doi.org/10.3390/met11030404>
- Choirotin, I., & Choiron, M. A. (2018). Defect Prediction at the superplastic forming process of the bipolar plate by simulation. *JEMME*, 3, 49–54. <https://doi.org/10.22219/jemmmme.v3i1.5884>

21. Zhong, J., Hou, B., Zhang, W., Guo, Z. S., & Zhao, C. W. (2023). Investigation on the physical and electrochemical properties of typical Ni-based alloys used for the bipolar plates of proton exchange membrane fuel cells. *Heliyon*, 9(5), 16276. <https://doi.org/10.1016/j.heliyon.2023.e16276>
22. Yeh, M. S., Tsau, C. W., & Chuang, T. H. (1996). Evaluation of the superplastic formability of SP-Inconel 718 superalloy. *Journal of Materials Engineering and Performance*, 5, 71–77. <https://doi.org/10.1007/BF02647272>
23. Şap, E., Usca, Ü. A., & Şap, S. (2024). Impacts of environmentally friendly milling of Inconel-800 superalloy on machinability parameters and energy consumption. *International Journal of Precision Engineering and Manufacturing-Green Technology*, 11, 781–797. <https://doi.org/10.1007/s40684-023-00579-4>
24. Yang, X., Wang, B. X., Jiang, W., Chen, S. N., & Wang, J. (2021). The superplasticity improvement of Inconel 718 through grain refinement by large reduction cold rolling and two-stage annealing. *Materials Science and Engineering: A*, 823(17), 141713. <https://doi.org/10.1016/j.msea.2021.141713>
25. Nguyen, T. A. N., Choi, H., Kim, M. J., Hong, S. T., & Han, H. N. (2022). Evaluation of efficiency of electrically assisted rapid annealing compared to rapid induction heat treatment. *International Journal of Precision Engineering and Manufacturing-Green Technology*, 9, 485–492. <https://doi.org/10.1007/s40684-021-00382-z>
26. Huang, L., Hua, P., Sun, W., Liu, F., & Qi, F. (2015). Necking characteristics and dynamic recrystallization during the superplasticity of IN718 superalloy. *Materials Science and Engineering: A*, 647, 277–286. <https://doi.org/10.1016/j.msea.2015.09.040>
27. Huang, L., Qi, F., Hua, P., Yu, L., Liu, F., Sun, W., & Hu, Z. (2015). Discontinuous dynamic recrystallization of inconel 718 superalloy during the superplastic deformation. *Metallurgical and Materials Transactions A*, 46, 4276–4285. <https://doi.org/10.1007/s11661-015-3031-0>
28. Wang, C., Xue, S., Chen, G., Cui, L. J., & Zhang, P. (2020). Investigation on formability of bipolar plates during flexible micro forming of Cu/Ni clad foils. *Journal of Manufacturing Processes*, 53, 293–303. <https://doi.org/10.1016/j.jmapro.2020.02.033>
29. Langdon, T. G. (2009). Seventy-five years of superplasticity: Historic developments and new opportunities. *Journal of Materials Science*, 44, 5998–6010. <https://doi.org/10.1007/s10853-009-3780-5>
30. Lee, H. T., & Hou, W. H. (2012). Fine grains forming process, mechanism of fine grain formation and properties of superalloy 718. *Materials Transactions*, 53(4), 716–723. <https://doi.org/10.2320/matertrans.M2011337>
31. Yang, X., Li, Z., Chen, S. N., Wang, B., Wang, B., Tian, Y., & Wang, J. (2024). Establishment and application of an internal-variable-based constitutive model for the superplastic deformation of Inconel 718 alloy. *Materials Science and Engineering: A*, 896, 146297. <https://doi.org/10.1016/j.msea.2024.146297>
32. Aue-U-Lan, Y., Ngaile, G., & Altan, T. (2004). Optimizing tube hydroforming using process simulation and experimental verification. *Journal of Materials Processing Technology*, 146(1), 137–143. [https://doi.org/10.1016/S0924-0136\(03\)00854-9](https://doi.org/10.1016/S0924-0136(03)00854-9)
33. Yang, X., Chen, S., Wang, B., Li, X., Wang, B., & Tian, Y. (2022). Superplastic deformation behavior of cold-rolled Inconel 718 alloy at high strain rates. *Journal of Materials Processing Technology*, 308, 117696. <https://doi.org/10.1016/j.jmatprotec.2022.117696>
34. Li, M., Pan, Q., Shi, Y., Sun, X., & Xiang, H. (2017). High strain rate superplasticity in an Al–Mg–Sc–Zr alloy processed via simple rolling. *Materials Science and Engineering: A*, 687(27), 298–305. <https://doi.org/10.1016/j.msea.2017.01.091>
35. Yasmeen, T., Zhao, B., Zheng, J. H., Tian, F., Lin, J. G., & Jiang, J. (2020). The study of flow behavior and governing mechanisms of a titanium alloy during superplastic forming. *Materials Science and Engineering: A*, 788(24), 139482. <https://doi.org/10.1016/j.msea.2020.139482>
36. Yasmeen, T., Shao, Z., Zhao, L., Gao, P., Lin, J. G., & Jiang, J. (2019). Constitutive modeling for the simulation of the superplastic forming of TA15 titanium alloy. *International Journal of Mechanical Sciences*, 164, 105178. <https://doi.org/10.1016/j.ijmecsci.2019.105178>
37. Lin, J., Liu, Y., Farrugia, D. C. J., & Zhou, M. (2005). Development of dislocation-based unified material model for simulating microstructure evolution in multipass hot rolling. *Philosophical Magazine*, 85(18), 1967–1987. <https://doi.org/10.1080/14786430412331305285>
38. Zhu, C., Harrington, T., Gray, G. T., III., & Vecchio, K. S. (2018). Dislocation-type evolution in quasi-statically compressed polycrystalline nickel. *Acta Materialia*, 155(15), 104–116. <https://doi.org/10.1016/j.actamat.2018.05.022>
39. Sato, E., & Kuribayashi, K. (1993). Superplasticity and deformation induced grain growth. *ISIJ International*, 33(8), 825–832. <https://doi.org/10.2355/isijinternational.33.825>

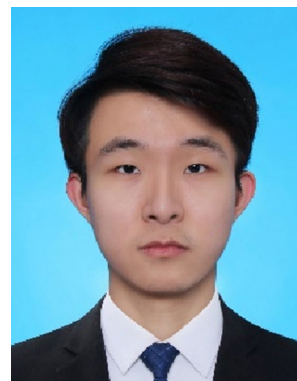
Publisher's Note Springer Nature remains neutral with regard to jurisdictional claims in published maps and institutional affiliations.

Springer Nature or its licensor (e.g. a society or other partner) holds exclusive rights to this article under a publishing agreement with the author(s) or other rightsholder(s); author self-archiving of the accepted manuscript version of this article is solely governed by the terms of such publishing agreement and applicable law.



Bingxing Wang Professor and Doctoral Supervisor at Northeastern University. Research has been conducted in the areas of metal material plastic forming and heat treatment processes, precision processing of ultra-thin strip materials for new energy applications, and forming technology for hydrogen fuel cell bipolar plates. Over 20 research projects have been undertaken, including those funded by the National Natural Science Foundation of China Youth Fund, National Defense Science and

Technology Industry Bureau Equipment Pre-research Fund, major science and technology planning projects in Liaoning Province, and significant enterprise R&D projects.



Yang Xu Doctor. The primary research focus is on the plastic deformation behavior and numerical simulation of metal foils. Involvement includes participation in various horizontal and vertical research projects.



Wenxiang Zhu Doctor. The primary research focus is on the plastic deformation behavior and numerical simulation of metal foils.



Zhuocheng Li The primary research focus is on the plastic deformation behavior and numerical simulation of metal foils.



Bin Wang Associate Professor and Doctoral Supervisor at Northeastern University. Dedicated to the research and development of new energy metal materials, optimization of precision processing for alloy materials, and cooling and heat treatment processes for highquality steel materials. He/she has led and participated in several national and provincial research projects, including the National Natural Science Foundation of China, Liaoning Provincial Natural Science Foundation, and

China Postdoctoral Science Foundation, as well as participating in the

“13th Five-Year Plan” National Key R&D Program and major projects of the National Natural Science Foundation.



Yong Tian Professor and Doctoral Supervisor at Northeastern University. Focused on advanced materials preparation technologies and the development of high-performance metal materials, has been involved in the development of China's first industrial-scale medium-thick plate ultra-fast cooling equipment, generating annual economic benefits exceeding 100 million yuan. Additionally, developed a rolling technology with low compression ratios and high permeability that breaks the

foreign monopoly. Achievements include one National Level Second-Class Award, two Provincial and Ministerial First-Class Awards, five Second-Class Awards, and one China Patent Excellence Award.